Triplets in the cradle: ultrafast dynamics in a cyclic disulfide

Electronic supplementary information (ESI)

James Merrick[a], Lewis Hutton[a], Joseph C. Cooper[a], Claire Vallance[a], Adam Kirrander[a]

Contents

A Electronic structure: benchmarking and geometry optimisation **2**
i. Electronic structure benchmarks 2
ii. Geometry optimisations 5

B Dynamics simulations **8**
i. Electronic state populations and nuclear dynamics 8
ii. Unsuccessful trajectories 8

—

[a] *Department of Chemistry, Physical and Theoretical Chemistry Laboratory, University of Oxford, South Parks Road, Oxford, OX1 3QZ, UK. Fax: +44 (0)1865 275400; Tel: +44 (0)1865 275400; E-mail: adam.kirrander@chem.ox.ac.uk*

A Electronic structure: benchmarking and geometry optimisation

i. Electronic structure benchmarks

The ANO-R1 basis set was used for all electronic structure calculations in the dynamics simulations on account of both its compactness and the fact that it is parametrised for scalar-relativistic effects.[1] Including scalar relativistic effects can allow for more accurate electronic structure calculations when comparatively heavy atoms — such as sulfur — are present in the molecule, since scalar relativistic effects scale as Z^4, where Z is the nuclear charge for a given atom.[2] Polarisation functions on all hydrogen atoms were removed from the basis in order to speed up the electronic structure calculations with only marginal cost to the accuracy; the duration of a single-point CASSCF(6,4) electronic structure calculation using the truncated basis set was approximately half the time compared to the full ANO-R1 basis set in an otherwise identical calculation — see Tab. A.1. The truncated basis set was benchmarked against a series of other basis sets across the LIIC pathway between the S_0(min) and S_1(min) geometries (see main article text); the approximate time taken per single-point CASSCF calculation for each basis set was recorded. This data is summarised in Table A.1, and the LIIC curves for each basis set are shown in Fig. A.1. The choice of basis only makes a marginal difference to the state energies (and their gradients with respect to the LIIC pathway) in Fig. A.1, and all vertical excitation energies and energy differences between optimised state minima in Table A.1 are very similar irrespective of basis set. This supports the decision to use the computationally efficient ANO-R1(t) basis set in the simulations.

Basis-set benchmarking: SA(4|4)-CASSCF(6,4)			
Basis set	ΔE $S_{0,FC}$-$S_{1,FC}$ / eV	ΔE S_0(min)-S_1(min) / eV	Wall clock time / s
ANO-R1(t)	4.50	2.03	19
ANO-R1	4.49	2.02	31
ANO-R2	4.45	2.11	390
def2-SV(P)	4.53	1.90	23
cc-pVDZ	4.41	1.92	75
aug-cc-pVDZ	4.50	2.08	220
cc-pVTZ	4.61	1.91	220
Experimental	**4.37**	—	—

Table A.1: Variation of: the $S_1 \leftarrow S_0$ vertical excitation energy in the Franck-Condon region (first column); the ground-state adiabatic excitation energy between the optimised S_0 and S_1 geometries (second column), and the approximate wall clock time taken per single-point CASSCF iteration across single-point calculations between optimised S_0 and S_1 geometries (final column). Electronic structure calculations were run on a single core on a compute node (Intel(R) Xeon(R) Gold 6326 CPU, 2.90 GHz). The experimental excitation energy, taken as the maximum of the S_1 absorption peak in the gas-phase absorption spectrum,[3,4] is provided for reference on the bottom row.

To justify the smaller (6,4) active space over the extended (10,8) active space (both active spaces are illustrated in the main article), the potential energy curves along the same LIIC with both active spaces are shown in Fig. A.1. Both sets of potential curves show qualitative and quantitative agreement, and the states calculated with the (10,8) active space have the same overall character in the Franck-Condon region as those calculated with the (6,4) active space (see Table A.2). This supports the choice of the smaller active space for the dynamics.

To validate the accuracy of using CASSCF as an electronic structure method for dynamics, LIIC potential curves between the S_0(min) and S_1(min) were calculated using CASSCF, and compared to LIIC curves calculated using MRCI and XMS-CASPT2. These curves are shown in Fig. A.2. The OpenMolcas v23.02 software package[5] was used for CASSCF and XMS-CASPT2 calculations, and the Molpro software package was used for MRCI calculations.[6] Fig. A.2 shows the small effect of removing hydrogen polarisation functions from the ANO-R1 basis set. One contributing factor to this is that the LIIC pathway between S_0(min) and S_1(min) mainly corresponds to stretching the S−S bond; the basis functions on the hydrogen atoms in the molecule are not expected to influence these energies much. Similarly, Fig. A.2 shows the negligible impact of varying the imaginary shift parameter in the expression for

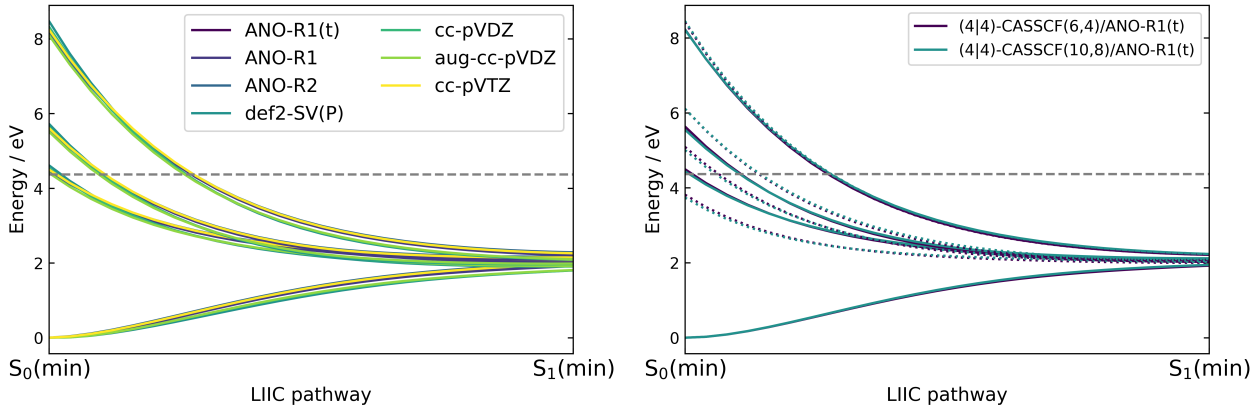

Figure A.1: (**Left**) LIIC potential energy curves for the four lowest-energy singlet states between S_0(min) and S_1(min) geometries optimised at the SA(4|4)-CASSCF(6,4)/ANO-R1(t) level of theory using different basis sets. The SA(4|4)-CASSCF(6,4) electronic structure method was used for each single-point calculation at each intermediate geometry. (**Right**) LIIC potential energy curves for the four lowest-energy singlet states (solid lines) and triplet states (dotted lines) between S_0(min) and S_1(min) geometries optimised at the SA(4|4)-CASSCF(6,4)/ANO-R1(t) level of theory using both a (6,4) active space (purple) and a (10,8) active space (green) for intermediate single-point electronic structure calculations. The dashed grey lines correspond to a best estimate of the experimental excitation energy from S_0 into S_1 in the Franck-Condon region (see Tab. A.1).

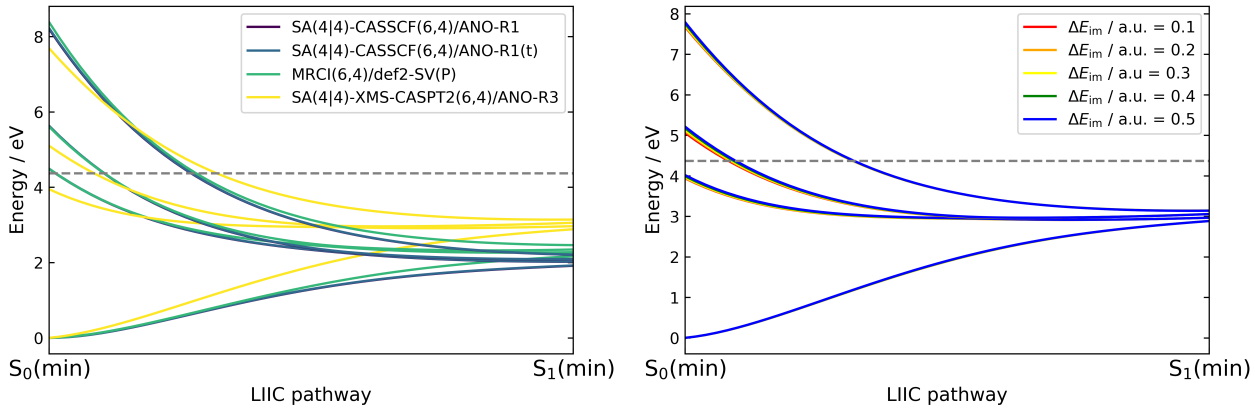

Figure A.2: (**Left**) LIIC potential energy curves for the four lowest-energy singlet states between S_0 and S_1 geometries optimised at the SA(4|4)-CASSCF(6,4)/ANO-R1(t) level of theory using CASSCF (red and orange), MRCI (green) and XMS-CASPT2 (blue) as electronic structure methods. XMS-CASPT2 calculations in (a) were performed using an imaginary level-shift of 0.2 Hartree. (**Right**) LIIC potential energy curves calculated on identical geometries as in (a), but performed at the SA(4|4)-XMS-CASPT2/ANO-R3 level of theory with varying imaginary level-shift parameters. The dashed grey lines in both plots correspond to a best estimate of the experimental excitation energy from S_0 into S_1 in the Franck-Condon region (see Tab. A.1).

Table A.2: State characters and associated CI-coefficients in the FC region for the four lowest-energy singlet and four lowest-energy triplet states of 1,2-dithiane calculated at the SA(4|4)-CASSCF(6,4)/ANO-R1(t) level of theory (**left**) and at the SA(4|4)-CASSCF(10,8)/ANO-R1(t) level of theory (**right**). Note that σ/σ^* orbitals in this table refer solely to the S-S bonding and antibonding orbitals of this symmetry; no C-S orbitals contribute significantly to the characters of the states shown when the (10,8) active space is used.

State	Dominant character	CI-coefficient
S_0	$(\sigma)^2(n_u)^2(n_g)^2$	0.980
S_1	$n_g\sigma^*$	0.954
S_2	$n_u\sigma^*$	0.911
S_3	$(n_g\sigma^*)(n_u\sigma^*)$	0.995
T_1	$n_g\sigma^*$	0.946
T_2	$n_u\sigma^*$	0.943
T_3	$\sigma\sigma^*$	0.984
T_4	$(n_g\sigma^*)(n_u\sigma^*)$	0.995

State	Dominant character(s)	CI-coefficient
S_0	$(\sigma)^2(n_u)^2(n_g)^2$	0.954
S_1	$n_g\sigma^*$	0.928
S_2	$n_u\sigma^*$	0.892
S_3	$(n_g\sigma^*)(n_u\sigma^*)$	0.960
T_1	$n_g\sigma^*$	0.921
T_2	$n_u\sigma^*$	0.918
T_3	$\sigma\sigma^*$	0.956
T_4	$(n_g\sigma^*)(n_u\sigma^*)$	0.963

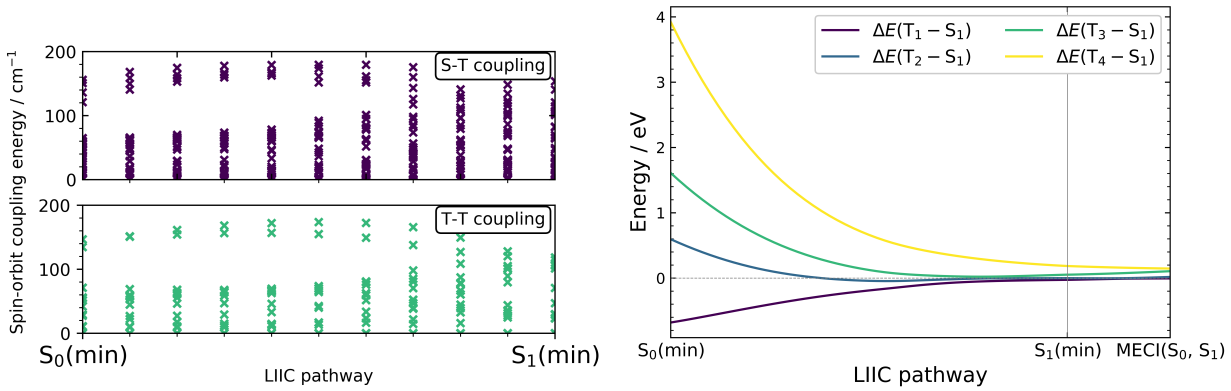

Figure A.3: (**Left**) All SOCMEs between all singlet-triplet state permutations (top) and triplet-triplet state permutations (bottom) along the LIIC pathway between the S_0(min) and S_1(min) geometries. Owing to the close structural similarity of the S_1(min) and MECI(S_0,S_1) geometries, only the LIIC pathway between S_0(min) and S_1(min) is shown for clarity. (**Right**) The energy gaps between the S_1 state and each triplet state manifold across the S_0(min) $\rightarrow$ S_1(min) $\rightarrow$ MECI(S_0, S_1) LIIC pathway.

the XMS-CASPT2 state energies (using otherwise the same XMS-CASPT2 method as shown in the left-hand plot in the same figure).

Whilst the CASSCF and MRCI LIIC curves are in good qualitative and quantitative agreement with each other, there is greater discrepancy between the CASSCF and XMS-CASPT2 LIIC curves. Notably, the XMS-CASPT2 results are also in poorer agreement with the best estimate for the experimental vertical excitation energy in the Franck-Condon region. Nonetheless, the *qualitative* behaviour of the LIIC curves for all the electronic structure methods included in Fig. A.2 all follow the same trend; the S_0 state characterises a potential well with respect to stretching the S$-$S coordinate, whereas all excited states are repulsive (dissociative) with respect to such a stretch, and the four lowest-energy singlet and triplet states are pseudo-degenerate in the limit of very large $r_{\mathrm{S-S}}$. Therefore, very similar dynamics can be expected irrespective of the electronic structure method used, albeit that the specific rate of population transfer and the exact Newton's cradle oscillation period may differ between CASPT2 and CASSCF due to differences in the gradients and the energies.

Finally, Fig. A.3 details all spin-orbit coupling (SOC) elements along the LIIC pathway coordinate from S_0(min) to S_1(min), as well as the energy gap between S_1 and the triplet state manifolds across the extended LIIC pathway. Notably, significant SOCs ($>$100 cm^{-1}) persist across the entire LIIC from a ring-closed geometry to a ring-opened geometry, thus supporting the notion that intersystem crossing (ISC) is expected to play a role in the early ring-opening dynamics of 1,2-dithiane.

ii. Geometry optimisations

S_0 (chair)			
S	-1.69349067	0.13947638	-2.10800565
S	-2.96436459	-1.01089036	-0.85037734
C	-1.67555555	-1.85699630	0.12121660
C	-0.80513841	-0.89506736	0.92770092
C	0.03803697	0.07300309	0.09082615
C	-0.76092938	1.01374326	-0.80918575
H	0.63657159	0.68218361	0.77246067
H	0.73978733	-0.49240153	-0.52502764
H	-1.44330318	-0.32885805	1.60855621
H	-0.12935554	-1.48805636	1.54870961
H	-1.45185332	1.62446314	-0.23141393
H	-0.08666006	1.68324049	-1.34386991
H	-2.21650657	-2.52492133	0.79203697
H	-1.07516663	-2.46873969	-0.54921491

S_1(min)			
S	-1.05759552	0.39228245	-2.53238146
S	-3.39999355	-1.27935203	-0.30079258
C	-1.75280738	-1.87587423	0.19465317
C	-0.83999100	-0.86983210	0.90228276
C	0.02446233	0.04917449	0.03158445
C	-0.70101610	1.06424426	-0.87173643
H	0.65298949	0.62524751	0.71312548
H	0.71147765	-0.55029593	-0.56855912
H	-1.43910658	-0.26778282	1.58631876
H	-0.14770673	-1.44351166	1.52388954
H	-1.63479473	1.38352380	-0.41570245
H	-0.06752884	1.93685517	-1.00733234
H	-1.96412218	-2.70581746	0.87039036
H	-1.27219685	-2.30868146	-0.68132811

MECI(S_0.S_1)			
S	-0.83076978	0.40577862	-2.58228452
S	-3.44372567	-1.24630033	-0.19094282
C	-1.77111878	-1.84762553	0.20246207
C	-0.82838890	-0.86685124	0.90836711
C	0.02821236	0.04370149	0.02081623
C	-0.73486002	1.04868189	-0.88026107
H	0.66968969	0.62334593	0.68435711
H	0.70410979	-0.56142185	-0.58479369
H	-1.40582605	-0.26424921	1.60921098
H	-0.13068717	-1.45638972	1.50839132
H	-1.71056128	1.26684249	-0.46130896
H	-0.15200233	1.96457290	-0.94383570
H	-1.95785425	-2.70116976	0.85668990
H	-1.32415760	-2.25874570	-0.70246796

S_0 (twist-boat)			
S	-0.40294075	-0.00649349	-0.38569519
S	-1.32350157	-1.91334685	-0.37230503
C	-3.07838604	-1.38751948	-0.42472077
C	-3.32655131	-0.10354756	-1.23392224
C	-2.37499290	0.08266476	-2.41868787
C	-0.97291739	0.57805480	-2.02649232
H	-2.28739891	-0.85637556	-2.96318853
H	-2.79996158	0.80616606	-3.11637846
H	-4.35591776	-0.13209879	-1.59505496
H	-3.25503494	0.75944487	-0.57356343
H	-0.24600202	0.30322176	-2.78707175
H	-0.96778090	1.66436145	-1.93543300
H	-3.59223076	-2.23059799	-0.88684741
H	-3.45945928	-1.27843991	0.58785348

Table A.3: Nuclear coordinates in Ångströms for the optimised molecular geometries corresponding to the S_0 lowest-energy conformation, which is a chair structure, (top left) and the S_1 minimum (top right), as well as the MECI(S_0,S_1) (bottom left) point, and finally, the higher-energy S_0 twist-boat molecular geometry. All structures are optimised at the SA(4|4)-CASSCF(6,4)/ANO-R1(t) level of theory.

The optimised geometries of the S_0 and S_1 states, as well as the MECI(S_0.S_1) point and the S_0 twist-boat local minimum, at the SA(4|4)-CASSCF(6,4)/ANO-R1(t) level of theory are detailed in Table A.3. The corresponding frequencies of all normal modes are provided in Table A.4. For completeness, we searched for additional state minima and MECIs. The results for these optimisation calculations are summarised with respect to the $r_{\mathrm{S-S}}$ and $\angle_{\mathrm{CCCC}}$ representative characteristic internal coordinates in Table A.5; note we were unable to locate certain MECIs.

To further justify using the SA(4|4)-CASSCF(6,4)/ANO-R1(t) electronic structure method for the simulations, the results of geometry optimisation calculations using a combination of different basis sets, active spaces, and electronic structure methods were compared. These are shown in Table A.6 and Table A.7 for CASSCF and XMS-CASPT2 optimisation calculations, respectively. MECI optimisation calculations were performed only once it had been decided that the (6,4) active space and the smaller ANO-R1 basis set was likely to be used for the dynamics.

Overall, when comparing the results of geometry optimisations between the CASSCF methods shown in Table A.6, there is very little variation in internal coordinates for a given state-optimised structure; there is minimal sensitivity

	Frequency / cm^{-1}			
Mode	S_0 (chair)	S_1(min)	S_0 (twist-boat)	MECI(S_0.S_1)
1	183.93	77.99	118.18	65.39
2	239.76	95.65	188.52	82.13
3	312.53	104.76	277.58	113.74
4	367.34	254.42	331.67	259.05
5	392.13	292.38	420.08	281.12
6	473.43	355.69	484.20	329.21
7	522.70	476.36	544.39	467.83
8	710.77	685.35	719.43	703.78
9	717.63	705.72	722.51	733.45
10	855.96	807.56	847.54	846.01
11	900.10	873.45	902.71	899.69
12	954.57	922.68	929.44	963.82
13	1006.39	991.26	1001.32	1021.09
14	1053.45	1068.04	1071.53	1130.92
15	1130.30	1133.15	1123.26	1154.68
16	1160.49	1174.39	1155.02	1162.76
17	1222.24	1220.29	1230.63	1257.21
18	1288.02	1307.89	1310.88	1332.17
19	1367.12	1362.82	1349.31	1366.24
20	1380.61	1372.56	1387.43	1395.40
21	1440.71	1440.29	1425.00	1437.30
22	1459.81	1451.48	1457.82	1449.96
23	1508.87	1513.82	1485.73	1509.27
24	1530.93	1532.56	1527.58	1527.20
25	1595.11	1580.15	1610.86	1619.23
26	1599.56	1614.02	1613.67	1624.20
27	1613.59	1620.29	1631.41	1635.16
28	1626.74	1629.50	1638.00	1662.73
29	3155.30	3158.18	3171.17	3160.62
30	3169.65	3177.02	3183.76	3177.59
31	3191.45	3188.73	3196.11	3185.06
32	3194.94	3205.94	3199.51	3203.30
33	3199.64	3216.71	3216.56	3213.52
34	3211.09	3224.24	3228.80	3224.02
35	3252.52	3245.53	3254.24	3229.23
36	3253.64	3283.87	3255.89	3300.07

Table A.4: Normal mode frequencies for the optimised geometries provided in Tab. A.3.

	S_2	S_3	T_1	T_2	T_3	T_4	MECI(S_1,S_2)	MECI(S_2,S_3)
$r_{\mathrm{S-S}}$ / Å	3.69	4.00	3.61	3.62	3.59	4.00	4.01	4.13
$\angle_{\mathrm{CCCC}}$ / °	65.1	61.0	69.4	63.2	63.8	61.2	62.6	61.0

Table A.5: Comparison of the $r_{\mathrm{S-S}}$ bond length and $\angle_{\mathrm{CCCC}}$ dihedral angle internal coordinates resulting from geometry optimisation calculations of additional state minima and MECIs.

	CASSCF(6,4)			CASSCF(10,8)	
	ANO-R1(t)	ANO-R1	ANO-R2	ANO-R1	ANO-R2
$r_{\mathrm{S-S}}$, S_0 / Å	2.13	2.13	2.10	2.13	2.10
$\angle_{\mathrm{CCCC}}$, S_0 / °	60.8	60.9	60.9	61.5	62.6
$r_{\mathrm{S-S}}$, S_1 / Å	3.64	3.64	3.64	3.65	3.68
$\angle_{\mathrm{CCCC}}$, S_1 / °	64.5	64.5	65.0	64.8	64.0
$r_{\mathrm{S-S}}$, MECI(S_0.S_1) / Å	3.91	3.91	—	3.95	—
$\angle_{\mathrm{CCCC}}$, MECI(S_0.S_1) / °	63.1	63.0	—	62.9	—

Table A.6: Comparison of the $r_{\mathrm{S-S}}$ bond length and $\angle_{\mathrm{CCCC}}$ dihedral angle internal coordinates resulting from geometry optimisation calculations of the S_0 and S_1 states in addition to the MECI(S_0.S_1) point using varied ANO-R basis sets and using either a (6,4) or (10,8) active space at the CASSCF level of theory.

	XMS-CASPT2(6,4)		XMS-CASPT2(10,8)	
	ANO-R1	ANO-R2	ANO-R1	ANO-R2
$r_{\mathrm{S-S}}$, S_0 / Å	2.08	2.04	2.09	2.05
$\angle_{\mathrm{CCCC}}$, S_0 / °	60.7	60.6	61.3	61.0
$r_{\mathrm{S-S}}$, S_1 / Å	3.37	3.23	3.37	3.25
$\angle_{\mathrm{CCCC}}$, S_1 / °	61.1	60.7	62.3	61.8

Table A.7: Comparison of the $r_{\mathrm{S-S}}$ bond length and $\angle_{\mathrm{CCCC}}$ dihedral angle internal coordinates resulting from geometry optimisation calculations of the S_0 and S_1 states in addition to the MECI(S_0.S_1) point using varied ANO-R basis sets and using either a (6,4) or (10,8) active space at the XMS-CASPT2 level of theory. An imaginary level-shift parameter of 0.2 Hartree was used for all calculations.

to both the basis and the active space used. For a given optimisation, $r_{\mathrm{S-S}}$ varies by less than 0.1 Å, and $\angle_{\mathrm{CCCC}}$ varies by less than 1° between different CASSCF methods. This supports using a smaller basis set and active space so as to minimise computational cost by excluding unnecessary orbitals and basis functions. It is also worthwhile to note that when holding all other parameters constant but using XMS-CASPT2 instead of CASSCF, the optimised ground-state structure changes very little. However, the geometry of the first excited state is more influenced by the choice of method.

—

B Dynamics simulations

i. Electronic state populations and nuclear dynamics

From an identical set of 8000 initial conditions, 384 trajectories were prepared for both trajectory ensembles. All dynamics was initiated on the S_1 state. Both sets of trajectories used the same random-number seed in setting up the trajectories. For the triplet-inclusive ensemble, 371/384 (96.6%) trajectories ran successfully (*i.e.* did not terminate prematurely due to any technical issues and reached the final time of $t = 1$ ps); for the singlet-only ensemble, 346/384 (90.1%) trajectories were successful. Fig. B.1 shows the individual electronic state populations — in the adiabatic state representation — for both trajectory ensembles across the total trajectory time.

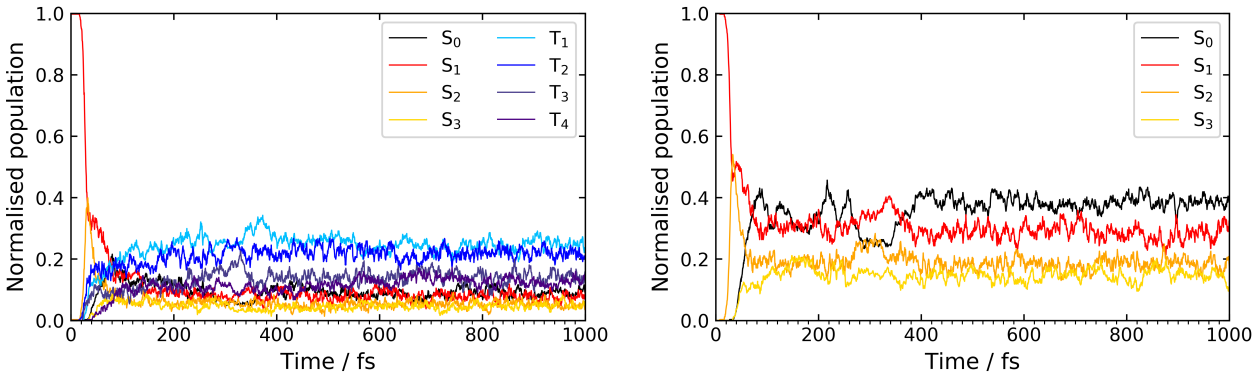

Figure B.1: The variation in MCH populations for separate MCH states for both the triplet-inclusive ensemble (**left**), where triplet states are summed over all three spin-orbit sub-states per state, and the singlet-only ensemble (**right**) across the total trajectory simulation time.

$$r_{\mathrm{S-S}} = A\sin(\frac{2\pi t}{T} + \phi)e^{-at} + c \tag{1}$$

Eq. (1) shows the fitting function used to fit the mean behaviour of $r_{\mathrm{S-S}}$ in both trajectory ensembles, and Table B.1 shows the fitting parameters (and their associated error, taken as one standard deviation above and below the mean value) calculated from the fitting procedure.

Table B.1: Fitting parameters and their errors for the fitting of the mean variation of $r_{\mathrm{S-S}}$ as a function of time for both trajectory ensembles. The damped sine function used to fit $r_{\mathrm{S-S}}$ is provided in Eq. 1.

Parameter	Triplet-inclusive ensemble	Singlet-only ensemble
T / fs	350.2 ± 1.1	351.1 ± 1.2
ϕ / rad	1.95 ± 0.01	1.96 ± 0.01
A / Å	-3.17 ± 0.01	-3.15 ± 0.01
c / Å	5.02 ± 0.01	4.98 ± 0.01
a / fs^{-1}	0.00200 ± 0.00005	0.00187 ± 0.00005

ii. Unsuccessful trajectories

An overview of the successful and unsuccessful trajectories for both ensembles is provided in Table B.2, including the reasons for why some trajectories were deemed 'unsuccessful'. A trajectory was marked as unsuccessful when at least one of the following criteria was true:

1. The trajectory was terminated prematurely (*i.e.* before it has been propagated for the total 1000 fs) by the SHARC program itself. This can happen as a result of failed electronic structure calls at a particular timestep,

which may itself be caused by the CASSCF calculation itself failing to converge at a particular geometry.

2. The total energy between the first and last timesteps was not conserved. This was flagged when the difference in the total energies between the first and last timesteps was greater than 0.2 eV.

3. The trajectory did not conserve energy between at least one pair of consecutive timesteps. This was flagged when the difference in energies between a pair of consecutive timesteps was greater than the 0.2 eV threshold.

Table B.2: Summary of trajectory success statistics for each ensemble. Note that the three causes of trajectories which were deemed unsuccessful are not mutually exclusive.

	Triplet-inclusive ensemble	Singlet-only ensemble
No. successful trajectories	**371**	**346**
No. unsuccessful trajectories	**13**	**38**
No. unsuccessful (terminated early)	7	12
No. unsuccessful (total energy not conserved)	3	20
No. unsuccessful (energy between timesteps not conserved)	5	25

Note that the three possible causes for why a trajectory may be unsuccessful are not mutually exclusive; for example, a given unsuccessful trajectory may have both energy conservation issues between timesteps and a net (total) energy conservation problem. A brief comparison of energy conservation issues between timesteps for both ensembles is provided below.

The triplet-inclusive and singlet-only trajectory ensembles yielded 5 and 25 trajectories which did not conserve energy between consecutive timesteps, respectively. For each such trajectories, both the molecular geometry - labelled henceforth as a "problematic" geometry for brevity - and the active state at the timestep(s) at which energy conservation was violated were extracted. Notably, all energy conservation violations occurred on the electronic ground state, and all corresponding geometries involved disulfide bond lengths either near to or compressed below the equilibrium bond distance of 2.13 Å for the ground state. The first observation reflects the inherent risk of instability in using CASSCF as an electronic structure method for propagating nuclear dynamics on a vibrationally hot ground state. To illustrate the latter observation, the value of $r_{\mathrm{S-S}}$ at all problematic geometries is plotted as a histogram alongside the minimum value of $r_{\mathrm{S-S}}$ for all successful trajectories from 200 fs onwards (Fig. B.2); all problematic geometries occurred at times greater than 200 fs, and the cut-off at 200 fs ensured that any minimum values of $r_{\mathrm{S-S}}$ resulting from the initial geometry at the start of the simulation were not included.

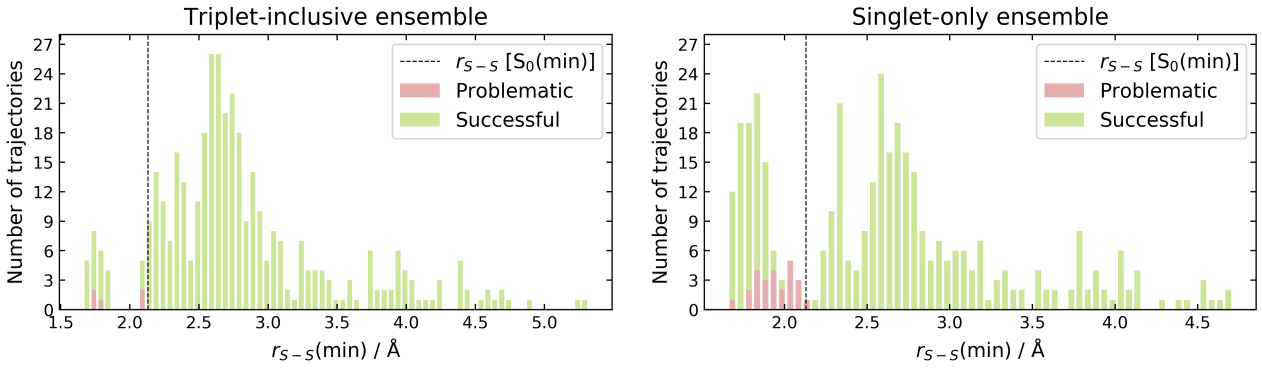

Figure B.2: A histogram of values of r_{S-S} corresponding for all problematic geometries and the minimum value of $r_{\mathrm{S-S}}$ for all successful trajectories from 200 fs until the end of the simulation time for the triplet-inclusive (**left**) and singlet-only (**right**). The value of $r_{\mathrm{S-S}}$ corresponding to the S$_0$(min) geometry is indicated in both plots.

Given that all unsuccessful trajectories were excluded from the analysis of bulk ensemble properties, care must be taken in analysing the probability of a given trajectory entering the ground state potential well and remaining there

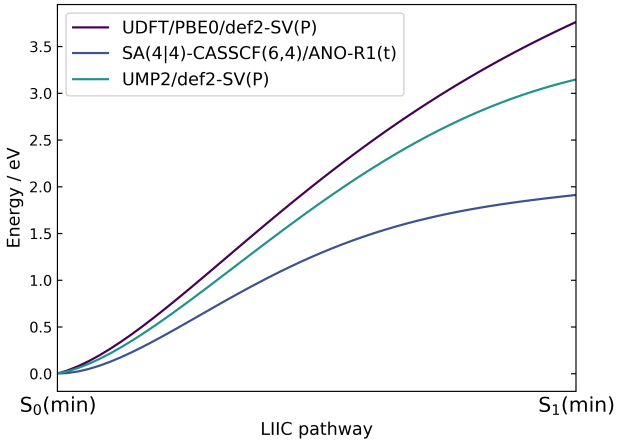

Figure B.3: A comparison of LIIC curves between the optimised S_0 and S_1 geometries at the: UDFT/PBE0/def2-SV(P) (**purple**); SA(4|4)-CASSCF(6,4)/ANO-R1(t) (**blue**), and UMP2/def2-SV(P) (**green**) levels of theory. The UDFT and MP2 calculations were performed using the ORCA (v5.0.3)[10,11] and TURBOMOLE(v7.6)[12] electronic structure software packages.

indefinitely for both ensembles since all energy conservation violations between timesteps in this study occur on the ground state and at ring-closed geometries. Restarting trajectories with a different electronic structure method just before encountering a problematic geometry - for example, using electronic structure methods which do not rely on an active space, such as unrestricted second-order Møller-Plesset perturbation theory (MP2)[7] or unrestricted density functional theory (DFT)[8] - was not performed since we were not able to identify an electronic structure method which gave a reliable (robust) description which also matched, qualitatively and quantitatively, the LIIC for the ground electronic state obtained by CASSCF. Indeed, both unrestricted MP2 and unrestricted DFT resulted in ground-state potential energy wells that were >1 eV deeper compared to CASSCF (Fig. B.3), meaning that electronic gradients at any point in configurational space on the ground state between CASSCF and such an alternative method were unlikely to be comparable. Further to this, by evaluating the D_1 diagnostic value[9] along the S_0/S_1 LIIC pathway, the reliability of a potential energy surface obtained by MP2 can be evaluated. The D_1 diagnostic is a measure of multireference character in the ground state at a particular geometry, where higher D_1 diagnostic values indicate a greater degree of multireference character. Generally, MP2 results where $D_1 \leq 0.015$ are taken to be reliable, whereas values in the range $0.015 \leq D_1 \leq 0.040$ must be analysed with more caution.[9] Given that D_1 is greater than 0.040 at geometries approaching the S_1 minimum geometry, unrestricted MP2 is likely to provide a poor description of the ground state potential energy surface in this region; thus, it was deemed unreliable to use this as a restarting method to gauge whether a trajectory would leave the ground state if restarted just before it encounters a problematic geometry when using CASSCF as a primary electronic structure method for dynamics.

References

(1) J. P. Zobel, P.-O. Widmark and V. Veryazov, *J. Chem. Theory Comput.*, 2020, **16**, 278–294.
(2) W. Liu, *Mol. Phys.*, 2010, **108**, 1679–1706.
(3) J. P. F. Nunes, Ph.D. Thesis, Chemistry, University of York, 2017.
(4) G. Bergson, G. Claeson, L. Schotte, A. Block-bolten, J. M. Toguri and H. Flood, *Acta Chem. Scand.*, 1962, **16**, 1159–1174.
(5) G. Li Manni, I. Fdez. Galván, A. Alavi, F. Aleotti, F. Aquilante, J. Autschbach, D. Avagliano, A. Baiardi, J. J. Bao, S. Battaglia, L. Birnoschi, A. Blanco-González, R. Broer, R. Cacciari, P. B. Calio, R. K. Carlson, R. Carvalho Couto, L. Cerdán, L. F. Chibotaru, N. F. Chilton, J. R. Church, I. Conti, S. Coriani, J. Cuéllar-Zuquin, R. E. Daoud, N. Dattani, P. Decleva, C. de Graaf, L. De Vico, W. Dobrautz, S. S. Dong, R. Feng, N.

Ferré, M. Filatov(Gulak), L. Gagliardi, M. Garavelli, L. González, Y. Guan, M. Guo, M. R. Hennefarth, M. R. Hermes, C. E. Hoyer, M. Huix-Rotllant, V. K. Jaiswal, A. Kaiser, D. S. Kaliakin, M. Khamesian, D. S. King, V. Kochetov, M. Krośnicki, A. A. Kumaar, E. D. Larsson, S. Lehtola, M.-B. Lepetit, H. Lischka, M. Lundberg, D. Ma, S. Mai, P. Marquetand, I. C. D. Merritt, F. Montorsi, M. Mörchen, A. Nenov, V. H. A. Nguyen, Y. Nishimoto, M. Olivucci, D. Padula, R. Pandharkar, Q. M. Phung, F. Plasser, G. Raggi, E. Rebolini, M. Reiher, D. Roca-Sanjuán, T. Romig, A. A. Safari, A. Sánchez-Mansilla, A. M. Sand, I. Schapiro, J. Segarra-Martí, F. Segatta, D.-C. Sergentu, P. Sharma, R. Shepard, J. K. Staab, T. P. Straatsma, L. K. Sørensen, B. N. C. Tenorio, D. G. Truhlar, L. Ungur, M. Vacher, V. Veryazov, T. A. Voß, O. Weser, D. Wu, X. Yang, D. Yarkony, C. Zhou, J. P. Zobel and R. Lindh, *J. Chem. Theory Comput.*, 2023, **19**, 6933–6991.

(6) H.-J. Werner, P. J. Knowles, F. R. Manby, J. A. Black, K. Doll, A. Heßelmann, D. Kats, A. Köhn, T. Korona, D. A. Kreplin, Q. Ma, T. F. Miller, III, A. Mitrushchenkov, K. A. Peterson, I. Polyak, G. Rauhut and M. Sibaev, *J. Chem. Phys.*, 2020, **152**, 144107.

(7) C. Møller and M. S. Plesset, *Phys. Rev.*, 1934, **46**, 618–622.

(8) K. Eichkorn, O. Treutler, H. Öhm, M. Häser and R. Ahlrichs, *Chem. Phys. Lett.*, 1995, **242**, 652–660.

(9) C. L. Janssen and I. M. Nielsen, *Chem. Phys. Lett.*, 1998, **290**, 423–430.

(10) F. Neese, *WIRES Comput. Molec. Sci.*, 2012, **2**, 73–78.

(11) F. Neese, *WIRES Comput. Molec. Sci.*, 2022, **12**, e1606.

(12) *TURBOMOLE V7.6 2022, a development of University of Karlsruhe and Forschungszentrum Karlsruhe GmbH, 1989-2007, TURBOMOLE GmbH, since 2007; available from* `https://www.turbomole.org`.